Crustal and upper mantle structure of southernmost South America inferred from regional waveform inversion

Stacey D. Robertson Maurice and Douglas A. Wiens
Department of Earth and Planetary Sciences, Washington University, St. Louis, Missouri, USA

Keith D. Koper
Department of Earth and Atmospheric Sciences, St. Louis University, St. Louis, Missouri, USA

Emilio Vera
Departamento de Geofisica, Universidad de Chile, Santiago, Chile

Received 11 February 2002; revised 12 July 2002; accepted 8 October 2002; published 24 January 2003.

[1] We determine the crustal and upper mantle structure of southern South America by inverting regional seismograms recorded by the Seismic Experiment in Patagonia and Antarctica. We present a waveform inversion method that utilizes a niching genetic algorithm. The niching genetic algorithm differs from the traditional genetic algorithm in that the inversion is performed in multiple subpopulations, thus generating a broader search of the model space and enabling us to examine alternative local error minima. The vertical and transverse waveforms were used, extending from the *P* arrival to the surface waves, and the inversion was performed at either 0.005–0.06 Hz (larger events) or 0.02–0.06 Hz (smaller events). The inversion included anisotropy by solving for separate *SV* and *SH* structures in the upper mantle. Results indicate that crustal thickness varies from 26 to 36 km with thicker values toward the northeast, suggesting that there is little crustal thickening beneath the austral Andes. The average upper mantle velocities are similar to the preliminary reference Earth model (PREM) except that the southernmost region shows velocities of 5% slower than PREM. The upper mantle has up to 5% polarization anisotropy between the Moho and 120 km depth. The strongest anisotropy is localized in a lithospheric lid shallower than 65 km depth, which overlies a pronounced low-velocity zone. This shallow limit to anisotropy is consistent with the relatively small shear wave splitting values found in this region. These results suggest that the anisotropy is limited to lithospheric depths and may imply the absence of a strong mantle flow pattern in the asthenosphere. *INDEX TERMS:* 3260 Mathematical Geophysics: Inverse theory; 7205 Seismology: Continental crust (1242); 7218 Seismology: Lithosphere and upper mantle; 7260 Seismology: Theory and modeling; 9360 Information Related to Geographic Region: South America; *KEYWORDS:* niching genetic algorithm, regional waveform inversion, South America, austral Andes, crustal structure, upper mantle structure

Citation: Robertson Maurice, S. D., D. A. Wiens, K. D. Koper, and E. Vera, Crustal and upper mantle structure of southernmost South America inferred from regional waveform inversion, *J. Geophys. Res.*, *108*(B1), 2038, doi:10.1029/2002JB001828, 2003.

1. Introduction

[2] Global and regional three-dimensional tomography are useful methods for mapping large-scale heterogeneities within the crust and upper mantle [e.g., *Montagner and Tanimoto*, 1991; *Woodward and Masters*, 1991; *Zhang and Tanimoto*, 1992; *Su et al.*, 1994; *Trampert and Woodhouse*, 1995]. However, in many cases, regions of the Southern Hemisphere are poorly resolved owing to poor path coverage, resulting in large resolution lengths (>10^3 km) [e.g., *Li and Romanowicz*, 1996; *Ekstrom and Dziewonski*, 1998]. Regional waveform inversion using data collected by temporary deployments allows some of these regions to be studied in more detail. Regional waveform inversion utilizes shorter path lengths compared to global tomographic studies, thus resulting in structure that is better localized in poorly sampled regions of the globe. In addition, regional waveform inversion can incorporate information from the entire seismic waveform, from the *P* arrival to the surface waves, and thus achieve good constraints on seismological structure over a wider depth range than surface wave or body wave inversion techniques alone.

[3] Waveform inversion is a traditional nonlinear optimization problem in that several local error minima exist within the model space. Therefore past regional waveform inversion methods utilizing linearized or gradient methods [*Nolet et al.*, 1986] have sometimes encountered consider-

0148-0227/03/2002JB001828$09.00

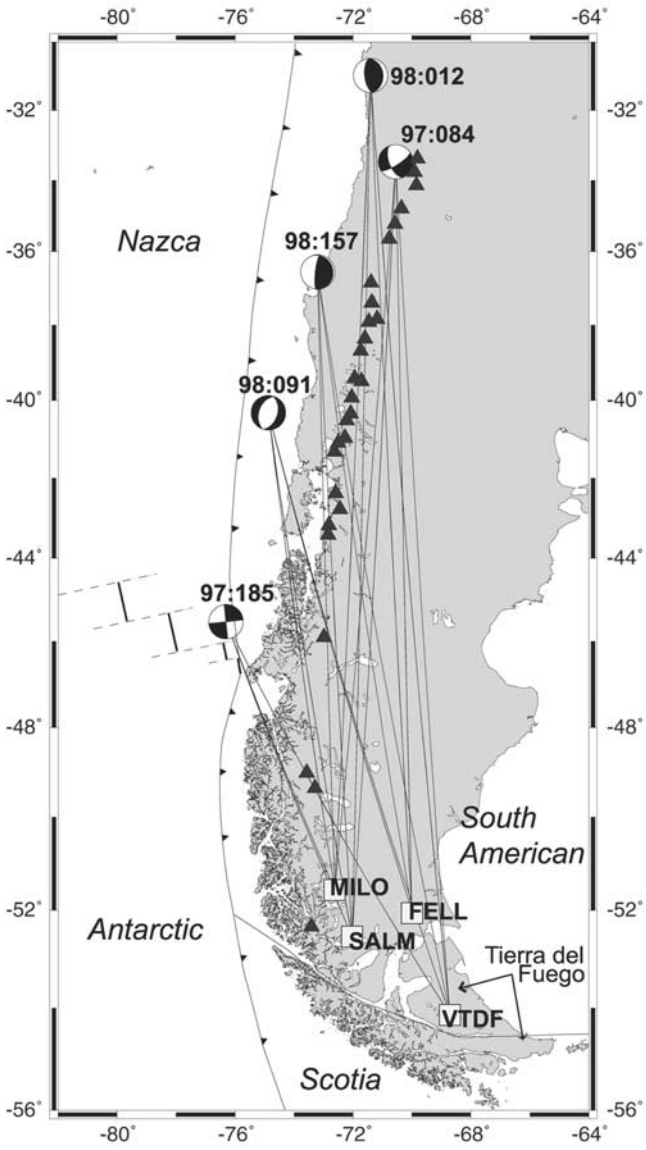

Figure 1. Map of South America with earthquakes shown as focal mechanisms and SEPA stations shown as squares. We chose earthquakes that were located to the north of our stations so that the paths would traverse the continent and the austral Andes. The events sample a range of locations and depths in order to examine a variety of paths. Event criteria included a high signal-to-noise ratio and a moment of greater than 8×10^{16} N m. Solid triangles indicate active volcanoes (Smithsonian Institution, Global Volcanism Program).

able nonuniqueness. Initial work attempting to invert the present data set using a conjugate gradient method developed by *Xu and Wiens* [1997] sometimes resulted in convergence to a local minimum, suggesting the need for a different method.

[4] In this study we develop a regional waveform inversion method using a niching genetic algorithm (NGA) [*Holland*, 1975; *Goldberg*, 1989; *Mahfoud*, 1995; *Koper et al.*, 1999], which allows us to explore the nonuniqueness of the inversion and offers a better opportunity to find the global error minima. Genetic algorithms are nonlinear optimization methods that utilize the processes of natural selection and natural genetics to breed solutions within a model space until the solution converges on an error minimum. The NGA differs from traditional genetic algorithms in that the model space is searched with distinct subpopulations, allowing for simultaneous identification of the global minimum and other high-quality local minima.

[5] We apply the NGA waveform inversion method to seismic data from paths traversing the austral Andes and southern South America. The events were recorded at four broadband stations, which were installed in Chilean Patagonia during 1997–1999 as part of the Seismic Experiment in Patagonia and Antarctica (SEPA). Earthquake and station locations are shown in Figure 1 [*Wiens et al.*, 1998].

2. Austral Andes and Southern South America

[6] The geological structure of southernmost South America is dominated by the Andean convergent margin, which has been the locus of ongoing convergence and magmatism since the Mesozoic [*Grunow et al.*, 1992]. Tectonics along this margin are currently controlled by the Nazca–South America–Antarctica triple junction, which is moving northward [*Cande and Leslie*, 1986] and which separates the fast subducting Nazca slab to the north from the much slower subducting Antarctic slab. Volcanism along the austral Andes south of the triple junction is less active than in the northern segment but extends essentially to the tip of South America (Figure 1). Early Paleozoic basement rocks dominate the Patagonian Massif to the east of the Andes [*Dalla Salda et al.*, 1992]. Geothermal gradients inferred from mantle xenoliths beneath southern Patagonia suggest a relatively thin continental lithosphere (less than 100 km thick) beneath this region [*Stern et al.*, 1999].

[7] Owing to its remote location and an absence of permanent seismic stations, few seismological studies have been carried out in this region, and knowledge of the lithospheric and crustal structure is incomplete. *Vdovin et al.* [1999] determined Rayleigh and Love wave group velocity maps for South America with a resolution length of ~1000 km and noted moderately slow long-period phase velocities beneath the Patagonia region. A waveform inversion study of South America suggests thickened crust (up to 60 km thick) and slow upper mantle velocities beneath the Andes near 35°S, but the study does not extend farther south owing to poor path coverage [*van der Lee et al.*, 2001]. Recent surface wave tomography of Antarctica and the surrounding regions shows the absence of a deep continental root beneath southernmost South America [*Danesi and Morelli*, 2001].

[8] Several studies suggest that the Andes in central South America show a thickened crust. At 20°S the Western Cordillera of the Altiplano has a crustal thickness of 70 km [*Beck et al.*, 1996]. Receiver function analysis of a recent broadband deployment near 36°S indicates that arc crust is 48–64 km thick and that the crust to the east of the volcanic arc is 32–40 km thick [*Beck et al.*, 2001]. However, it is not clear whether this thickened crust extends southward into the austral Andes. A seismic refraction experiment performed by *Ludwig et al.* [1965] determined that the crust is 40 km thick in northern Tierra del Fuego and 35 km thick

in southern Tierra del Fuego. Crustal model CRUST2.0 by G. Laske et al. (http://mahi.ucsd.edu/Gabi/rem.dir/crust/crust2.html) shows a crustal thickness of 30–40 km beneath southern South America, although this part of the model is constrained by very few data points [*Mooney et al.*, 1998].

3. Waveform Inversion Method

3.1. Previous Regional Waveform Inversion Methods

[9] A variety of methods may be used to determine seismic velocity structure through waveform inversion. Traditionally, the objective function is defined as the misfit between the synthetic seismogram and the data, so the best solution would generate the fit with absolute minimum error. Iterative linearized inversion is used when the structure is assumed to be a small variation from the starting model; the synthetic seismogram is expanded in a truncated Taylor series around the starting model [*Woodhouse and Dziewonski*, 1984]. The solution may converge on a local minimum if the starting model is not close enough to the actual structure. Gradient techniques include the steepest descent and conjugate gradient methods. Compared with the linearized inversion method, the nonlinear gradient method is less restrictive for the starting model, but it is still a local optimization method that requires a good a priori model. The gradient of the objective function is calculated, and the algorithm searches in the downhill direction to find the local objective function minima closest to the starting model. Given a good starting model the correct solution will be found, and this method has been used successfully in several cases [e.g., *Xu and Wiens*, 1997].

[10] Regional waveform inversion is strongly nonlinear, such that linearized or gradient methods do not effectively search the solution space and may converge on local minima. A grid search algorithm is not feasible for an inversion with such a large parameter space. This suggests that global optimization methods such as simulated annealing [*Rothman*, 1985; *Kirkpatrick et al.*, 1983] or genetic algorithms [*Goldberg*, 1989; *Stoffa and Sen*, 1991] may be particularly useful. Here we develop a niching genetic algorithm inversion method for regional waveforms that offers a particularly effective method for searching the model space.

3.2. Niching Genetic Algorithm

[11] Genetic algorithms (GA) are randomized search algorithms based on the processes of natural selection and natural genetics. The basic genetic algorithm uses three operators: reproduction, crossover, and mutation. The algorithm first produces a given number of random models; the value of each model parameter must fall within limits set by the user. The parameters may be represented using either binary or floating point; in this case we chose floating point because it allows for a more complete search of the model space. Once the models of the first generation are randomly determined, the reproduction function is implemented by assigning fitness function values to each model [*Sambridge and Drijkoningen*, 1992]. The models with higher fitnesses will be more likely to breed and pass their traits to the next generation, whereas those with low fitness values will be quickly eliminated from the selection process. Fitness computations are based only on the relative error of each model. Use of such a rank-based method eliminates the need for fitness scaling and often increases the overall efficiency of the GA search. After the models are bred, the crossover function is implemented and some models undergo mutation. After the genetic algorithm runs for a number of generations it will converge on a solution that produces an error minimum [*Goldberg*, 1989; *Stoffa and Sen*, 1991].

[12] A disadvantage of the genetic algorithm is that like other global optimization techniques it is not guaranteed to find the solution with the global error minimum. Although it is unlikely that the solution will converge on a local minimum as long as the size of the population and the probability of crossover and mutation are chosen wisely [*Stoffa and Sen*, 1991], in practice, this can lead to unreasonable amounts of computation. Running competing, parallel genetic algorithms on several different model populations helps to solve the problem of premature convergence on a local minimum. Each group acts as a subpopulation which seeks a niche in the model space. Therefore such an algorithm is termed a ''niching genetic algorithm'' [*Holland*, 1975; *Goldberg*, 1989; *Mahfoud*, 1995; *Koper et al.*, 1999]. In our NGA implementation a penalty function forces the best solutions in each subpopulation to differ from one another, effectively requiring the subpopulations to explore separate portions of the model space. The NGA is thus fundamentally different than simply rerunning a GA multiple times because the subpopulations compete with each other.

[13] A well-parameterized NGA will eventually determine the global minimum, and it will also allow examination of the best solutions in each subpopulation in order to determine whether several different solutions can provide similar results. This is helpful when performing waveform inversions because we can evaluate various trade-offs that exist in our models. Our NGA included five subpopulations, each of which contained 20 models. Therefore 100 models were evaluated in each generation. The smaller earthquakes, inverted over smaller frequency bands, were inverted for 400 generations and the larger events for 700 generations. Significant changes in the resulting models rarely took place after 400 generations, but we allowed the extra run time to be certain we had found the best solutions.

[14] The degree to which a solution will be penalized for similarity to the solutions in other subpopulations is termed the critical radius of separation, or R_c. If $R_c = 0$, then all of the subpopulations will converge to the global minimum because they are allowed to be similar. If the value of R_c is too high, subpopulations become frustrated because they are too similar to the first subpopulation and are not permitted to search the model space. A moderate value of R_c will allow the different subpopulations to sample local minima and yet not converge too close to the global minimum. The R_c value used in our inversion was 0.2.

3.3. NGA Implementation

3.3.1. Model Parameterization

[15] For our waveform inversion we assumed a layered, laterally homogeneous model and solved for crustal thickness, seismic velocities, and polarization anisotropy. We parameterized the model using the shear wave velocity in each layer as the fundamental set of unknowns since the

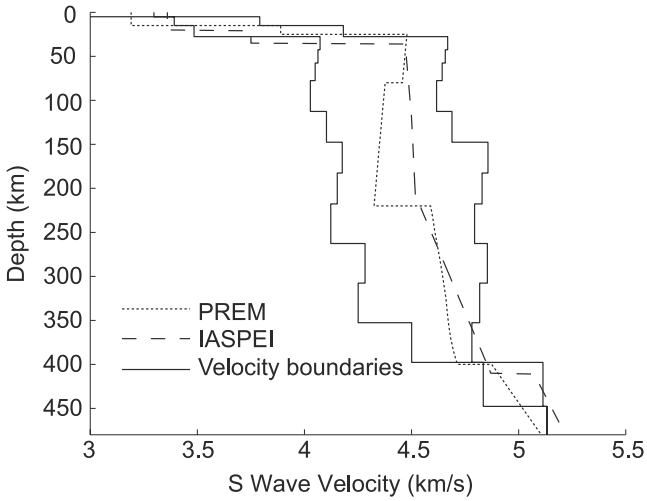

Figure 2. Plot showing isotropic PREM velocities, International Association of Seismology and Physics of the Earth's Interior (IASPEI) velocities, and the *SV* velocity limits used for the inversion.

regional waveforms are dominated by the *S* wave and surface waves that are most sensitive to shear velocity. The *P* velocity for each layer is derived from the relationship $\alpha = \gamma\beta$, where γ is the ratio of *P* velocity to *S* velocity. We used the preliminary reference Earth model (PREM) values to determine the α/β ratio, and the density of each layer was calculated from the formula $\rho = \rho_0 + 0.32(\alpha\text{-}\alpha_0)$, where ρ_0 and α_0 are the density and *P* velocities of the PREM model, respectively [*Berteussen*, 1977; *Dziewonski and Anderson*, 1981]. These approximations for the *P* velocity and density will have a relatively small effect on the waveforms since the waveforms are most sensitive to the shear velocity.

[16] We solved for the velocities of 15 layers, including three crustal layers, which extend to a total depth of 480 km. The layer thicknesses of the structure were held constant except for the bottom layer of the three-layer crust. The thickness of the layers ranged from 5 km for the uppermost crust to 53.6 km for the deepest mantle layer. Initial isotropic inversions showed that the vertical and transverse waveforms could not be matched by a single velocity model and that upper mantle polarization anisotropy was required. Therefore we allowed the transverse (*SH*) and vertical (*SV*) structures to differ in the upper seven layers of the mantle down to a depth of ~225 km. A weak penalty function, described in section 3.3.2, provided a slight bias in favor of an isotropic model to ensure than any anisotropy in the resulting models was actually required by the data. We assigned a single value of anisotropy to several mantle layers in order to reduce the number of anisotropy parameters to three. The final inversion solved for 19 parameters, including the velocity of the top 15 layers, the thickness of the lower crust, and three parameters describing the degree of polarization anisotropy in the top seven layers of the mantle.

[17] We set appropriate limits for each parameter solved for in the inversion based on previous studies on the structure of South America. If any of our runs resulted in a best fit model that included either the maximum or minimum limit of any parameter, we then expanded the bounds so that the solution was not restricted. We allowed the crustal thickness to vary between 20 and 45 km. Velocity boundaries for each layer were chosen such that velocity tended to increase with depth, but low velocity zones were still possible (Figure 2). Anisotropy for each layer in the upper mantle was allowed to reach a maximum of 9%. The *SH* structure was assumed to be faster than the *SV* structure, as was observed in preliminary isotropic modeling and is generally observed worldwide [*Dziewonski and Anderson*, 1981; *Gaherty*, 2001]. Although it is possible that crustal anisotropy exists in the southernmost part of South America [*Helffrich et al.*, 2002], we did not feel that the degree of anisotropy within the crust was large enough to incorporate those additional parameters into our inversion.

3.3.2. Synthetic Seismograms and the Objective Function

[18] The primary component of the objective function was the root-mean-square residual between the synthetic and recorded seismograms in the time domain. Synthetics were calculated using a reflectivity method [*Kennett*, 1983; *Randall*, 1994]. This method does not allow anisotropy to be explicitly included in the velocity structure, so we computed the transverse synthetics separately from the vertical synthetics. We did not use the radial component seismograms as they have lower signal-to-noise ratios and do not provide much additional information relative to the vertical component seismograms. The use of separate *SH* and *SV* structures to compute the transverse and vertical synthetics is a good approximation to a truly anisotropic structure and is commonly made for polarization anisotropy [e.g., *Webb and Forsyth*, 1998]. We tested this approximation using a wave number integration code developed by R. B. Herrmann (http://www.eas.slu.edu/People/RBHerrmann/ComputerPrograms.html) to produce synthetics for a transversely isotropic (TI) structure approximately equivalent to our separate *SH* and *SV* structures. We found that synthetics calculated using the TI code were essentially identical to those calculated using separate *SH* and *SV* structures. Six additional layers extending from 480 to 780 km depth with velocities from PREM [*Dziewonski and Anderson*, 1981] were added to the bottom of the structure, resulting in 21 layers for the synthetic computation. Since there are few data on attenuation in this region, synthetics were calculated using the PREM attenuation model. We performed forward modeling tests for different attenuation values and found that the results are not sensitive to reasonable variations in the attenuation model.

[19] We inverted the entire waveform extending from the *P* arrival through the surface waves to obtain the maximum resolution of structure through a wide depth range since the surface waves are more sensitive to shallow structure and the body waves provide better constraints at deeper depths. We required larger earthquakes to fit the data within two different frequency bands, 0.005–0.02 Hz and 0.02–0.06 Hz. Inverting the data in two separate frequency bands provides better constraints on the deeper structure and ensures that the low-frequency data are given similar weight to higher-frequency data, which are more prominent in the raw displacement records. Data that showed poor signal-to-noise characteristics at long periods, generally from smaller

Table 1. Parameters of Earthquakes Used in the Inversion

Julian Date	Calendar Date	Time, UT	Latitude	Longitude	Depth, km	M_w
97:084	25 March 1997	0014:44.6	−33.48	−70.55	84	5.5
97:185	4 July 1997	2352:04.5	−45.53	−76.31	10	5.2
98:012	12 Jan. 1998	1014:07.6	−30.99	−71.41	34	6.6
98:091	1 April 1998	2242:56.9	−40.32	−74.87	9	6.7
98:157	6 June 1998	1216:18.8	−36.56	−73.20	23	5.2

earthquakes, were inverted within a single-frequency band of 0.02–0.06 Hz. Tests comparing two-frequency band inversions with a single-frequency band inversion for the same data showed that the differences were small and nonsystematic. We also incorporated a second derivative smoothing penalty and a weighted anisotropy penalty. The smoothing penalty increased the objective function value for solutions with profiles containing anomalously slow or fast velocity layers, thus reducing the likelihood of unrealistic models fitting the data. The smoothing penalty was small enough that low- or high-velocity zones were allowed, but rough models with alternating fast and slow layers would be more quickly eliminated. The anisotropy penalty added an error directly proportional to the total amount of anisotropy in the model. Therefore a model with no anisotropy would have the lowest penalty, and we could ensure that anisotropy would exist in our models only if required. The final objective function value was the sum of the transverse and vertical errors at both frequency bands after incorporating the penalty functions, and we called this value the cost.

4. Application to Southern South America

4.1. Data

[20] The data used for our waveform inversions were from the Seismic Experiment in Patagonia and Antarctica. Twelve broadband Program for Array Seismic Studies of the Continental Lithosphere (PASSCAL) seismometers were deployed between 1997 and 1999 in Antarctica and Chilean Patagonia. Each station consisted of a Streckeisen STS 2 sensor in a vault and a Reftek 24-bit data acquisition unit with a GPS clock. The four Patagonian stations used in this study recorded data continuously at either 25 or 40 samples per second.

[21] There is a high level of seismicity along the western coast of South America owing to the subducting Nazca and Antarctic slabs. We focused our study on earthquakes that were located to the north of our stations, so that the paths would traverse the continent and the austral Andes. We chose events that sampled a range of locations and depths in order to examine a variety of paths. Event criteria included a high signal-to-noise ratio and a seismic moment greater than 8×10^{16} N m. The events were between 720 and 2600 km from the stations. The locations and depths of the earthquakes in this study were taken from the preliminary determination of epicenters (PDE) monthly bulletin, and the focal mechanisms were taken from the Harvard centroid moment tensor (CMT) catalog [*Dziewonski et al.*, 1981]. The percent velocity error due to possible mislocation can be calculated by dividing the epicentral uncertainty by the distance from the source to the seismometer. If we assume that the PDE epicenter errors are ~10 km for events with $M_w \sim 6$ and that the depth errors for these events are <10 km based on comparison with Harvard CMT solutions, the station distances ranging from 720 to 2600 km suggest location-related errors in our velocities of between 0.4% and 1.4%. Event parameters are listed in Table 1, and the paths covered by the event-station pairs are shown in Figure 1.

Table 2. High-Quality Results of Event-Station Pairs Used in This Study[a]

	MILO	SALM	FELL	VTDF
97:084	X	X	XX	XX
97:185	X	X		X
98:012	X	XX	XX	XX
98:091	XX	XX	XX	XX
98:157	X	X	X	

[a]X, event-station pairs with high-quality inversion results at low frequencies; XX, event-station pairs with high-quality inversion results at low and high frequencies.

4.2. Results

[22] A total of 40 source-receiver inversions were performed, 20 at the 0.02–0.06 Hz frequency band only and 20 at both the 0.005–0.02 Hz and 0.02–0.06 Hz bands. The result of each inversion was evaluated based on the fit of the synthetic seismograms to the data, and models showing large costs were excluded. Large costs were seen for the two-frequency inversions of the smallest earthquakes (Julian dates 97:185 and 98:157) and for some of the inversions from the 97:084 and 98:012 events due to a lower signal-to-noise ratio at long periods. Other large misfits might result from modeling stations near nodes in the Rayleigh or Love radiation patterns and from off-azimuth surface wave arrivals. The remaining high-quality results used in this study are indicated by an "X" in Table 2.

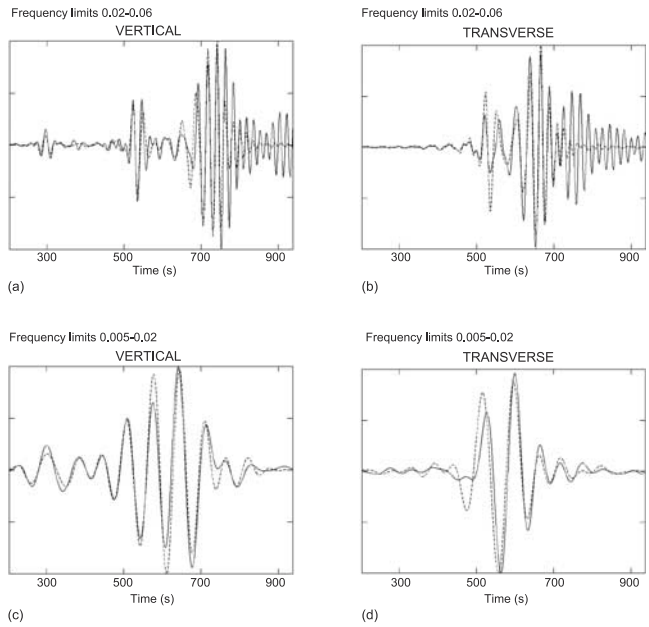

Figure 3. Observed data and synthetic seismogram for earthquake 98:012, recorded at station FELL. (a and b) High-frequency and (c and d) low-frequency data were inverted simultaneously. The solid line represents the data, and the dotted line is the synthetic seismogram.

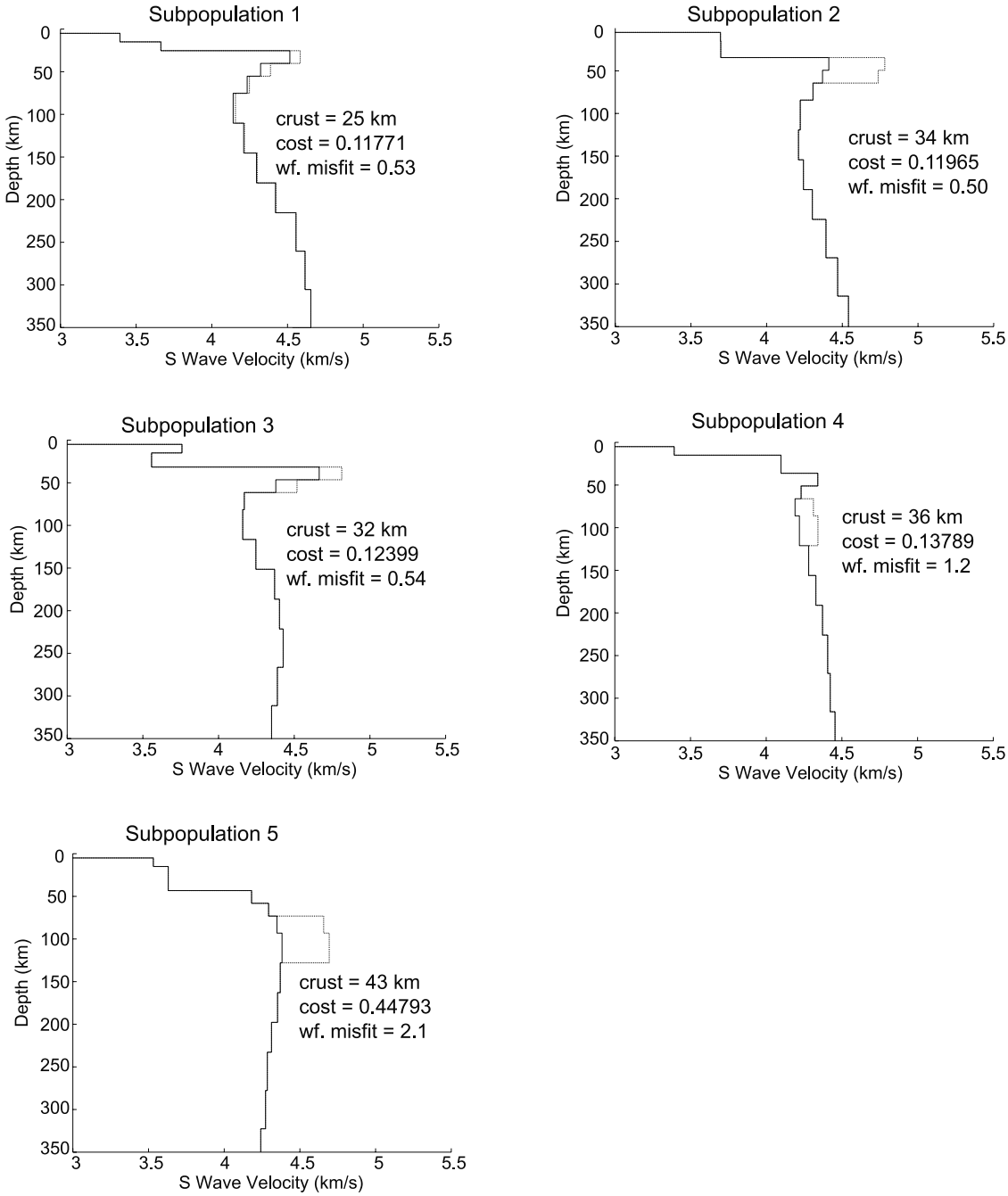

Figure 4. *SV* and *SH* velocity profile solutions of the subpopulations for the 98:091 earthquake recorded at station FELL. Solid lines indicate *SV* velocity structure, and dotted lines indicate *SH* velocity structure. Labels indicate crustal thickness, cost, and waveform misfit.

Attempts at simultaneously inverting a few of the larger earthquakes indicated that the records could not be fit by a single velocity structure owing to lateral heterogeneity and possible small source location errors.

[23] The waveforms from one niching genetic algorithm inversion are shown in Figure 3. This event took place on 12 January 1998 and had a depth of 34 km. The fit between the data and the synthetic seismogram is excellent on both the vertical and transverse components for both frequency bands and is typical of the fits for other earthquake inversions in this study.

[24] Figure 4 shows the final velocity models for each of the subpopulations calculated for the 98:091 event at FELL station. The first solution shows a 25-km-thick crust and 1.5% anisotropy in the uppermost 40 km of the mantle. The second model has more anisotropy (8.4%) and a thicker crust (34 km). A trade-off between layer thickness and velocity is shown clearly here, as the solution with a thicker crust shows slower average upper mantle velocities. The difference in waveform misfit between the first and second subpopulations for this path was exceptionally small compared to most of the inversions. In fact, the waveform misfit

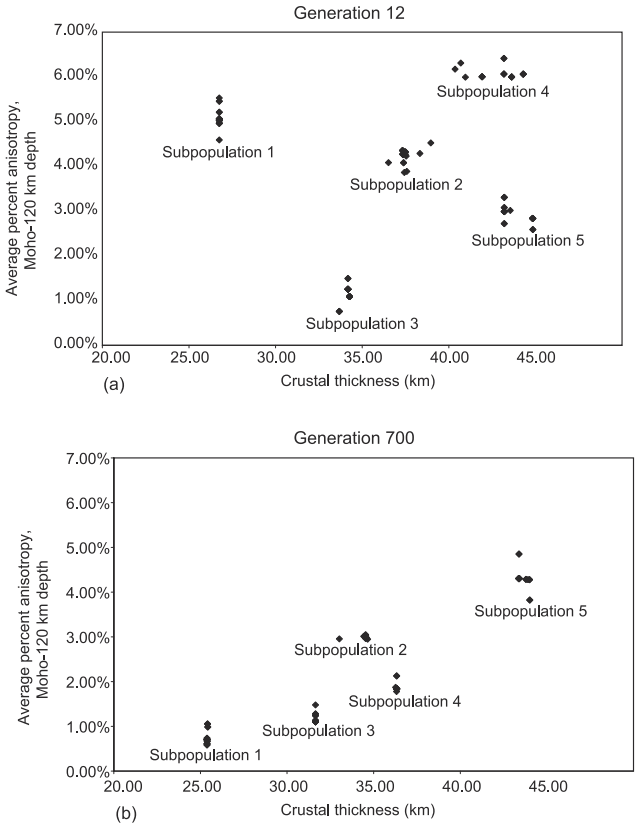

Figure 5. 98:091 models plotted at generations (a) 12 and (b) 700, showing average anisotropy versus crustal thickness. The clusters of models represent the different subpopulations. Each subpopulation consists of 20 models, but not all models are visible because they have identical discrete values of crustal thickness and anisotropy. As a whole, the subpopulations migrated toward values of lower anisotropy over the course of the inversion.

for the second subpopulation is actually less than the misfit for the first subpopulation, and the increase in cost for the second subpopulation is largely an effect of the anisotropy penalty. The second subpopulation solution might even be the preferred solution for this path because it is more similar to the best solutions from the other inversions. There were only a few paths for which we found the second subpopulation's waveform misfit to be almost identical to or better than that of the first subpopulation. To avoid prejudice, we always used the solution from the first subpopulation in our analysis, but these results illustrate the use of the NGA in providing insight to alternative local minima providing a good fit to the data. They also suggest that the crustal thickness and anisotropy are not well resolved by these data, but all successful models do require some anisotropy. The solution from the third subpopulation is similar to the first two solutions, but there is an anomalously fast layer in the crust. This solution was likely eliminated in part because the second derivative smoothness penalty function increased its cost. The fourth and fifth subpopulations show smooth velocity profiles but produce much higher waveform misfits than the other subpopulations.

[25] Figure 5 shows the clustering of the solutions in each subpopulation for generations 12 and 700 of the 98:091 event. The plot shows average anisotropy versus crustal thickness and disregards the other parameters of the inversion. It is interesting to observe that the subpopulations are, in fact, distinct from one another and migrate within the model space over time. The amount of anisotropy in the models decreased from generation 12 to generation 700.

4.3. Discussion

[26] Our results show that crustal thickness in the region varies from 26 to 36 km (Figure 6). It is thus much thinner than the 70-km thickness observed in the Altiplano region to the north of the study area [*Beck et al.*, 1996] and the 48–64 km thick crust found along the volcanic arc near 36°S [*Beck et al.*, 2001]. These results demonstrate that little crustal thickening has occurred south of about 36°S in the Andes, providing useful constraints on models of compressional shortening and magmatic accretion in the southern Andes. Paths from the 97:185 event sample the austral Andes south of the triple junction and southwest of the other paths and indicate thinner crust (26 km) compared to paths sampling the pre-Cambrian platform and Andes farther to the north (32–36 km). This suggests rather thin crust beneath the southernmost austral Andes.

[27] We qualitatively evaluated the resolution of our crustal thickness by examining the different subpopulations and their costs. Examination of the waveforms showed that the visual appearance of the waveform fit was significantly worse when the difference in cost between the best subpopulation and the subpopulation in question was >0.1. After eliminating these poor solutions, 79% of the remaining solutions had a crustal thickness within 8 km of the best model's crustal thickness. We therefore conclude that our crustal thickness is accurate to within ~8 km, and the crust in southern South America is indeed thinner than the crust in central South America and the Altiplano region.

[28] Overall, the solutions show upper mantle velocities that are slightly slow relative to PREM. Figure 7a shows

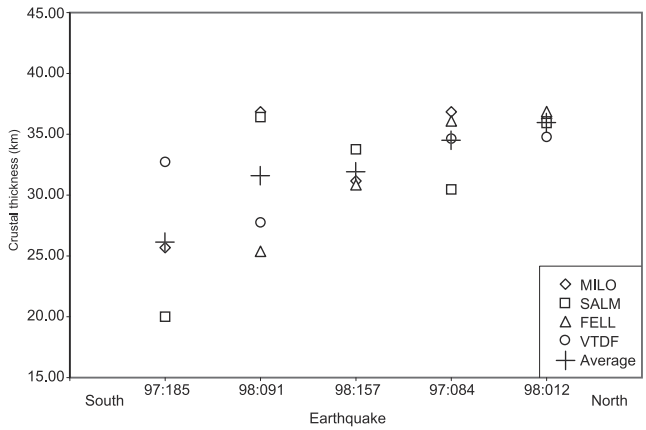

Figure 6. Crustal thicknesses calculated for each event, with earthquakes plotted so that the westernmost paths are on the left side of the graph. The two-frequency results are plotted if they contained good long-period signals; otherwise, the high-quality one-frequency results are shown. The results from the two-frequency runs are similar to those from the one-frequency runs and indicate a slight increase in crustal thickness from west to east.

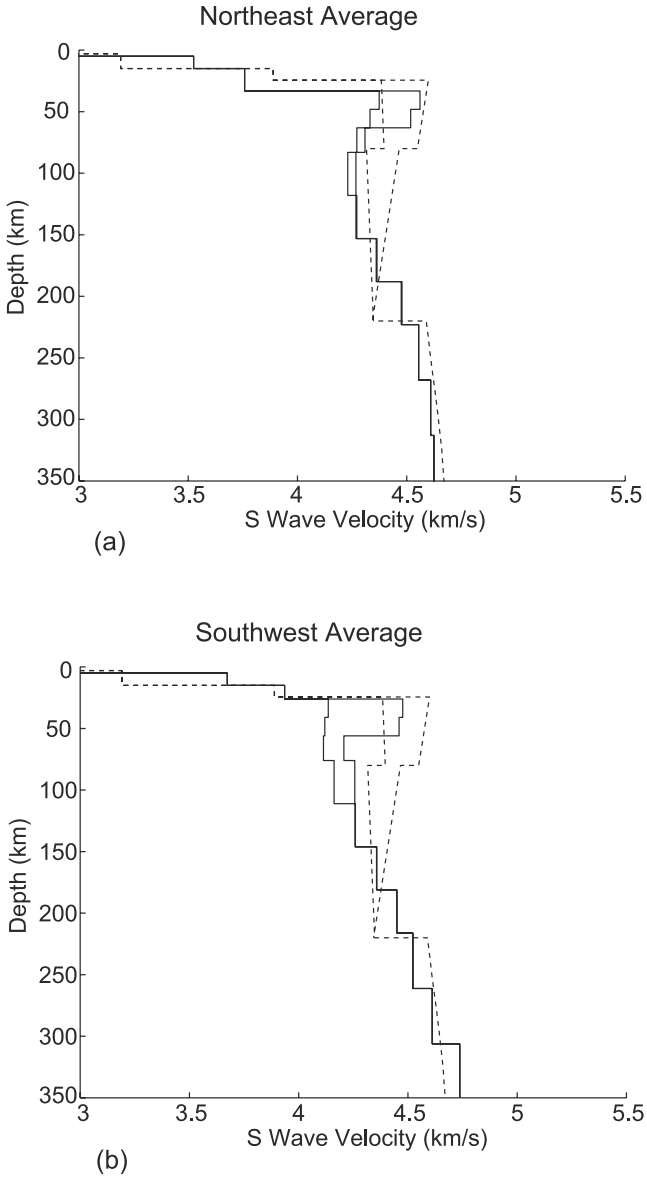

Figure 7. (a) Plot showing the average result from the four northern events. (b) Plot showing the average result from the southernmost event (97:185). Note the thin lithosphere lid extending to 60 km depth and the anisotropy focused in the upper 60 km but extending no deeper than 120 km. The dotted line indicates PREM velocities.

the average solution for the four northern events, and Figure 7b shows the average structure for the southernmost event (97:185) in comparison with PREM. These structures are also shown in Table 3. The average *SV* velocities from the Moho to 120 km depth are shown in Figure 8. The average *SV* velocities fall in the range of 4.3–4.4 km/s with the exception of the 97:185 event, which has slower velocities. The paths traversed by this event are located to the southwest relative to the paths for the other events (Figure 1). Therefore this earthquake samples the material in the mantle wedge in the region where the young Antarctic plate is subducting at very low velocity. Young subduction zones have generally elevated temperatures, and the signatures of slab melts have been detected in young adakite

Table 3. Average Models

Depth, km	*SV* velocity, km/s	*SH* velocity, km/s
	Northeastern Events	
5	2.87	2.87
15	3.53	3.53
34	3.78	3.78
49	4.41	4.60
64	4.38	4.56
84	4.33	4.37
120	4.31	4.35
155	4.37	4.38
191	4.49	4.50
227	4.64	4.64
274	4.75	4.75
321	4.85	4.85
369	4.90	4.90
	Southwestern Event	
5	2.76	2.76
15	3.68	3.68
26	3.95	3.95
41	4.16	4.51
56	4.16	4.50
77	4.16	4.26
112	4.24	4.33
148	4.36	4.36
184	4.48	4.49
220	4.60	4.61
267	4.72	4.72
314	4.84	4.84
361	5.01	5.01

lavas in the austral Andes south of 48°S, suggesting that the slow velocities in this region result from elevated mantle temperatures [*Sigmarsson et al.*, 1998]. There is no geochemical evidence of slab melting north of the triple junction, suggesting that the path traversed by the 97:185 event is indeed much warmer than the other paths. *Morris* [1998] suggests that the temperatures here could be between 800°C and 1,150°C, several hundred degrees hotter than predicted for most subducting slabs. Patagonian xenoliths also indicate elevated temperatures in this region

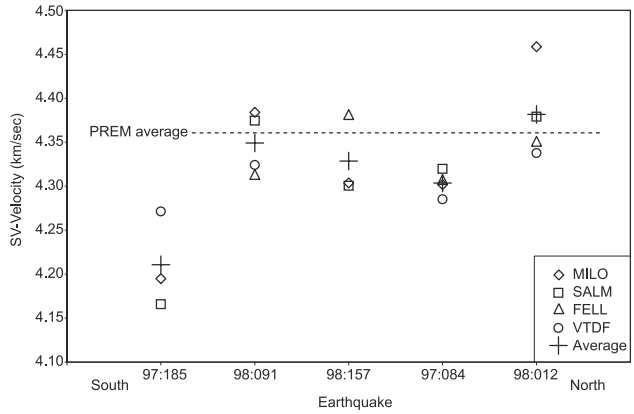

Figure 8. Average *SV* velocity from the Moho to 120 km depth. For records with good long-period signals we plot the two-frequency band inversion results, whereas the single-band results are plotted for noisier records. There is no systematic difference between the two-frequency and one-frequency results. The average *SV* velocity is between 4.3 and 4.4 km/s except for the westernmost event, 97:185, which shows slower upper mantle velocities.

accompanied by thinning of the lithosphere [*Stern et al.*, 1999].

[29] The average velocity models (Figure 7) show a rather thin lithospheric lid with some anisotropy, which extends from the Moho to ~60 km depth. Below this depth the amount of anisotropy is reduced, and a low-velocity zone extends to depths of ~150 km. Velocities in the low-velocity zone are up to 5% slower than PREM for the southwestern paths. It is interesting that even the easternmost paths, which sample early Paleozoic continental lithospheres, show a thin lid extending to only 60 km depth and a prominent low-velocity zone. This is consistent with mantle xenolith observations whose temperatures and pressures indicate a thin continental lithosphere and the absence of a cratonic root in this region [*Stern et al.*, 1999]. They are also consistent with tomographic results showing the absence of a deep continental root beneath southernmost South America [*Danesi and Morelli*, 2001].

[30] The amount of anisotropy averaged between the Moho and 120 km depth was between 0.5% and 5% for all the event-station paths. We do not see any prominent regional trends in anisotropy, but it is clear that regional, upper mantle anisotropy is present. The amount and precise depth range of the anisotropy were not well resolved owing to trade-offs with crustal thickness and mantle velocity structure. However, inversions without anisotropy resulted in poor fits for either the vertical or transverse waveforms, indicating that the anisotropy above 120 km is necessary. By performing forward modeling tests we found that the waveforms were indeed sensitive to anisotropy between 120 and 220 km depth. The fact that the anisotropy was not present at these depths in our models indicates that anisotropy does not extend beneath the mantle lid in this region. The models indicate that the strongest anisotropy, ranging from 2 to 9%, is present in the lithospheric lid extending from the Moho to 60 km depth. Only weak anisotropy of <2% is present between 60 and 120 km depth, and no anisotropy occurs beneath 120 km. This suggests that anisotropy is largely confined to the lithospheric lid and that little anisotropy occurs in the asthenosphere.

[31] Seismic anisotropy in the upper mantle is generally thought to result from preferred orientation of olivine induced by strain [*Nicolas and Christensen*, 1987; *Mainprice and Silver*, 1993]. This strain can be caused by a variety of mechanisms, including mantle flow induced by absolute plate motion [*Tanimoto and Anderson*, 1984], small-scale convection, or horizontal flow caused by mantle plumes [*Ekstrom and Dziewonski*, 1998]. It can also result from lithospheric fabric frozen into position from past episodes of deformation [*Silver*, 1996]. In the case of South American anisotropy, *Russo and Silver* [1994] proposed that mantle anisotropy in the western central area of the continent was caused by forced mantle flow around the subducting Nazca slab into the Atlantic. This model suggests that flow should continue along the strike of the South American slab into Drake Passage or escape to the Atlantic beneath the short austral Andes slab in the study area. However, shear wave splitting analysis using the SEPA stations in southern South America revealed very little azimuthal anisotropy and fast directions perpendicular to what would be expected from mantle flow around the subducting slab [*Helffrich et al.*, 2002]. A larger degree of seismic anisotropy was observed at seismometers located between 45.4°S and 46.6° S in Chile, but the anisotropy in this area can be attributed to the local subduction of the Chile Rise spreading ridge [*Murdie and Russo*, 1999].

[32] In this study, we observe polarization anisotropy largely limited to depths shallower than 80–120 km, at the depths of the lithospheric lid. This is consistent with lithospheric anisotropy, in which strong anisotropy is confined to the uppermost continental mantle. Although these polarization anisotropy measurements are not directly comparable with *SKS* splitting studies that measure azimuthal anisotropy, the small splitting times are also compatible with anisotropy confined to lithospheric depths [*Helffrich et al.*, 2002]. Both studies suggest a general absence of strong asthenospheric flow patterns beneath southern South America.

5. Conclusions

[33] The application of the NGA waveform inversion method to waveforms traversing southernmost South America has increased our understanding of this remote region. The basic conclusions of this study can be summarized as follows:

1. The niching genetic algorithm is a useful method for performing regional waveform inversion for crustal and upper mantle structure. No a priori model is required, and the niching algorithm forces the inversion to search the entire model space to find the best model with a relatively low chance of becoming caught in a local minima.

2. The crustal thickness ranges from 26 to 36 km, indicating that the crustal thickening observed farther north in the Altiplano region is not present south of about 36°S. There is some evidence that the crust thickens slightly from southwest to northeast.

3. The velocity structures determined through our inversions indicate upper mantle velocities up to 5% slower than PREM. The structures show a thin lithospheric lid extending only to depths of 60 km, consistent with previous mantle xenolith studies indicating a thin continental lithosphere. The southwesternmost paths show slower average velocities in the upper mantle, most likely due to sampling of the warm austral Andes volcanic arc.

4. The upper mantle has up to 5% polarization anisotropy between the Moho and 120 km depth. Inversions performed without allowing for anisotropy were unable to fit the data well, thus indicating that anisotropy is an important component of the upper mantle. Anisotropy is not present beneath 120 km, and is most prominent in the lithospheric lid between the Moho and 60 km depth. The shallow depth is consistent with anisotropy limited to lithospheric depths and with relatively small shear wave splitting values found in this region and suggests the absence of a strong mantle flow pattern.

[34] **Acknowledgments.** The PASSCAL program of the Incorporated Research Institutions in Seismology (IRIS) provided equipment for the SEPA deployment. We thank Patrick Shore, George Helffrich, Gonzalo Perez, Sergio Barrientos, Paul Friberg, and Rodrigo Adaros for their assistance in deploying and maintaining the seismic stations in Patagonia. We also thank George Randall for the use of his reflectivity code, Bob Herrmann for the use of his TI code, and Suzan van der Lee for her helpful comments. This project was supported by the National Science Foundation under grants OPP-9527366 and OPP-9814622 and by a National Science Foundation Graduate Fellowship.

References

Beck, S., G. Zandt, S. C. Myers, T. C. Wallace, P. G. Silver, and L. Drake, Crustal thickness variations in the central Andes, *Geology*, *24*, 407–410, 1996.

Beck, S., et al., CHARGE, the CHile ARgentina Geophysical Experiment: Imaging the south central Andean lithosphere using passive broadband seismology (abstract), *Eos Trans. AGU*, *82*(47), Fall Meet. Suppl., Abstract T31A-0828, 2001.

Berteussen, K., Moho depth determinations based on spectral-ratio analysis of NORSAR long-period P waves, *Phys. Earth Planet. Inter.*, *15*, 13–27, 1977.

Cande, S. C., and R. B. Leslie, Late Cenozoic tectonics of the southern Chile Trench, *J. Geophys. Res.*, *91*, 471–496, 1986.

Dalla Salda, L., C. Cingolani, and R. Varela, Early Paleozoic orogenic belt of the Andes in southwestern South America: Result of Laurentia-Gondwana collision?, *Geology*, *20*, 617–620, 1992.

Danesi, S., and A. Morelli, Structure of the upper mantle under the Antarctic Plate from surface wave tomography, *Geophys. Res. Lett.*, *28*, 4395–4398, 2001.

Dziewonski, A. M., and D. L. Anderson, Preliminary reference Earth model, *Phys. Earth Planet. Inter.*, *25*, 297–356, 1981.

Dziewonski, A. M., T.-A. Chou, and J. H. Woodhouse, Determination of earthquake source parameters from waveform data for studies of global and regional seismicity, *J. Geophys. Res.*, *86*, 2825–2852, 1981.

Ekstrom, G., and A. Dziewonski, The unique anisotropy of the Pacific upper mantle, *Nature*, *394*, 168–172, 1998.

Gaherty, J. B., Seismic evidence for hotspot-induced buoyant flow beneath the Reykjanes Ridge, *Science*, *293*, 1645–1647, 2001.

Goldberg, D. E., *Genetic Algorithms in Search, Optimization, and Machine Learning*, 412 pp., Addison-Wesley-Longman, Reading, Mass., 1989.

Grunow, A. M., I. W. D. Dalziel, T. M. Harrison, and M. T. Heizler, Structural geology and geochronology of subduction complexes along the margin of Gondwanaland: New data from the Antarctic Peninsula and southernmost Andes, *Geol. Soc. Am. Bull.*, *104*, 1497–1514, 1992.

Helffrich, G., D. A. Wiens, E. Vera, S. Barrientos, P. Shore, S. Robertson, and R. Adaros, A teleseismic shear-wave splitting study to investigate mantle flow around South America and implications for plate-driving forces, *Geophys. J. Int.*, *149*, F1–F7, 2002.

Holland, J. H., *Adaptation in Natural and Artificial Systems: An Introductory Analysis With Applications to Biology, Control, and Artificial Intelligence*, 183 pp., Univ. of Mich., Ann Arbor, Mich., 1975.

Kennett, B. L. N., *Seismic Wave Propagation in Stratified Media*, 342 pp., Cambridge Univ. Press, New York, 1983.

Kirkpatrick, S., C. D. Gelatt, and M. P. Vecchi, Optimization by simulated annealing, *Science*, *220*, 671–680, 1983.

Koper, K. D., M. E. Wysession, and D. A. Wiens, Multimodal function optimization with a niching genetic algorithm: A seismological example, *Bull. Seismol. Soc. Am.*, *89*, 978–988, 1999.

Li, X.-D., and B. Romanowicz, Global mantle shear velocity model developed using nonlinear asymptotic coupling theory, *J. Geophys. Res.*, *101*, 22,245–22,272, 1996.

Ludwig, W. J., J. I. Ewing, and M. Ewing, Seismic-refraction measurements in the Magellan Straits, *J. Geophys. Res.*, *70*, 1855–1876, 1965.

Mahfoud, S. W., Niching methods for genetic algorithms, Ph.D. thesis, Univ. of Ill. at Urbana-Champaign, Urbana, 1995.

Mainprice, D., and P. G. Silver, Interpretation of SKS-waves using samples from the subcontinental lithosphere, *Phys. Earth Planet. Inter.*, *78*, 257–280, 1993.

Montagner, J. P., and T. Tanimoto, Global upper mantle tomography of seismic velocities and anisotropies, *J. Geophys. Res.*, *96*, 20,337–20,351, 1991.

Mooney, W. D., G. Laske, and T. G. Masters, CRUST 5.1: A global crustal model at 5° × 5°, *J. Geophys. Res.*, *103*, 727–747, 1998.

Morris, J. D., Hot stuff under southern Chile, *Nature*, *394*, 523–524, 1998.

Murdie, R. E., and R. M. Russo, Seismic anisotropy in the region of the Chile margin triple junction, *J. S. Am. Earth Sci.*, *12*, 261–270, 1999.

Nicolas, A., and N. I. Christensen, Formation of anisotropy in upper mantle peridotites: A review, in *Composition, Structure and Dynamics of the Lithosphere-Asthenosphere System*, *Geodyn. Ser.*, vol. 16, edited by K. Fuchs and C. Froidevaux, pp. 111–123, AGU, Washington, D.C., 1987.

Nolet, G., J. van Trier, and R. Huisman, A formalism for nonlinear inversion of seismic surface waves, *Geophys. Res. Lett.*, *13*, 26–29, 1986.

Randall, G. E., Efficient calculation of complete differential seismograms for laterally homogeneous Earth models, *Geophys. J. Int.*, *118*, 245–254, 1994.

Rothman, D. H., Nonlinear inversion, statistical mechanics, and residual statics estimation, *Geophysics*, *50*, 2784–2796, 1985.

Russo, R. M., and P. G. Silver, Trench-parallel flow beneath the Nazca Plate from seismic anisotropy, *Science*, *263*, 1105–1111, 1994.

Sambridge, M., and G. G. Drijkoningen, Genetic algorithms in seismic waveform inversion, *Geophys. J. Int.*, *109*, 323–342, 1992.

Sigmarsson, O., H. Martin, and J. Knowles, Melting of a subducting oceanic crust from U-Th disequilibria in austral Andean lavas, *Nature*, *394*, 566–569, 1998.

Silver, P. G., Seismic anisotropy beneath the continents: Probing the depths of geology, *Annu. Rev. Earth Planet. Sci.*, *24*, 385–432, 1996.

Stern, C. S., R. Kilian, B. Olker, E. H. Hauri, and T. K. Kyser, Evidence from mantle xenoliths for relatively thin (<100 km) continental lithosphere below the Phanerozoic crust of southernmost South America, *Lithos*, *48*, 217–235, 1999.

Stoffa, P. L., and M. K. Sen, Nonlinear multiparameter optimization using genetic algorithms: Inversion of plane-wave seismograms, *Geophysics*, *56*, 1794–1810, 1991.

Su, W., R. L. Woodward, and A. M. Dziewonski, Degree 12 model of shear velocity heterogeneity in the mantle, *J. Geophys. Res.*, *99*, 6945–6980, 1994.

Tanimoto, T., and D. L. Anderson, Mapping convection in the mantle, *Geophys. Res. Lett.*, *11*, 287–290, 1984.

Trampert, J., and J. H. Woodhouse, Global phase velocity maps of Love and Rayleigh waves between 40 and 150 seconds, *Geophys. J. Int.*, *122*, 675–690, 1995.

van der Lee, S., D. James, and P. Silver, Upper mantle *S* velocity structure of central and western South America, *J. Geophys. Res.*, *106*, 30,821–30,834, 2001.

Vdovin, O., J. A. Rial, A. L. Levshin, and M. H. Ritzwoller, Group-velocity tomography of South America and the surrounding oceans, *Geophys. J. Int.*, *136*, 324–340, 1999.

Webb, S. C., and D. W. Forsyth, Structure of the upper mantle under the East Pacific Rise from waveform inversion of regional events, *Science*, *280*, 1227–1229, 1998.

Wiens, D., S. Robertson, G. Smith, P. Shore, E. Vera, S. Barrientos, and G. Perez, Seismic experiment in Patagonia and Antarctica, *IRIS Newsl.*, *7*, 9–11, 1998.

Woodhouse, J. H., and A. M. Dziewonski, Mapping the upper mantle: Three-dimensional modeling of Earth structure by inversion of seismic waveforms, *J. Geophys. Res.*, *89*, 5953–5986, 1984.

Woodward, R. L., and G. Masters, Global upper mantle structure from long-period differential travel times, *J. Geophys. Res.*, *96*, 6351–6377, 1991.

Xu, Y., and D. A. Wiens, Upper mantle structure of the southwest Pacific from regional waveform inversion, *J. Geophys. Res.*, *102*, 27,439–27,452, 1997.

Zhang, Y.-S., and T. Tanimoto, Ridges, hotspots, and their interaction as observed in seismic velocity maps, *Nature*, *355*, 45–49, 1992.

K. D. Koper, Department of Earth and Atmospheric Sciences, Macelwane Hall, St. Louis University, 3507 Laclede Ave., St. Louis, MO 63103, USA. (koper@eas.slu.edu)

S. D. Robertson Maurice and D. A. Wiens, Department of Earth and Planetary Sciences, Washington University, 1 Brookings Dr. #1169, St. Louis, MO 63130, USA. (stacey@seismo.wustl.edu; doug@kermadec.wustl.edu)

E. Vera, Departamento de Geofisica, Facultad de Ciencias Físicas y Matemáticas, Universidad de Chile, Casilla 2777, Santiago, Chile. (evera@dgf.uchile.cl)